

Instability of a Noncrystalline NaO_2 Film in $\text{Na}-\text{O}_2$ Batteries: The Controversial Effect of the RuO_2 Catalyst

Mohammad Fathi Tovini,[†] Misun Hong,[‡] Jiwon Park,[‡] Merve Demirtaş,[§] Daniele Toffoli,^{||} Hande Ustunel,[§] Hye Ryung Byon,^{‡,⊥} and Eda Yilmaz^{*,†}

[†]Institute of Materials Science and Nanotechnology, National Nanotechnology Research Center, Bilkent University, Ankara 06800, Turkey

[‡]Department of Chemistry, Korea Advanced Institute of Science and Technology (KAIST), 291 Daehak-ro, Yuseong-gu, Daejeon 34141, Republic of Korea

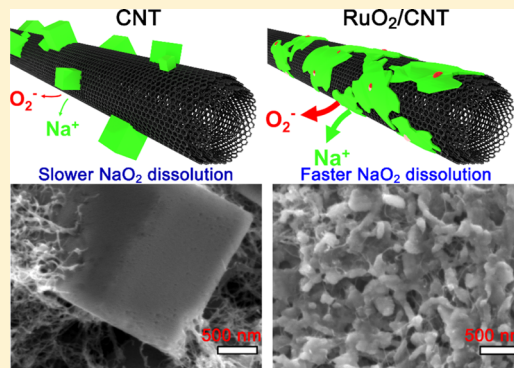
[§]Department of Physics, Middle East Technical University, Dumlupinar Bulvari 1, 06800 Ankara, Turkey

^{||}Dipartimento di Scienze Chimiche e Farmaceutiche, Università degli Studi di Trieste, Via L. Giorgieri 1, I-34127 Trieste, Italy

[⊥]Advanced Battery Center, KAIST Institute NanoCentury, 291 Daehak-ro, Yuseong-gu, Daejeon 34141, Republic of Korea

Supporting Information

ABSTRACT: The unique electrochemical and chemical features of sodium–oxygen ($\text{Na}-\text{O}_2$) batteries distinguish them from the lithium–oxygen ($\text{Li}-\text{O}_2$) batteries. NaO_2 as the main discharge product is unstable in the cell environment and chemically degrades, which triggers side products' formation and charging potential increment. In this study, RuO_2 nanoparticles dispersed on carbon nanotubes (CNTs) are used as the catalyst for $\text{Na}-\text{O}_2$ batteries to elucidate the effect of the catalyst on these complex electrochemical systems. The RuO_2/CNT contributes to the formation of a poorly crystalline and coating-like NaO_2 structure during oxygen reduction reaction, which is drastically different from the conventional micron-sized cubic NaO_2 crystals deposited on the CNT. Our findings demonstrate a competition between NaO_2 and side products' decompositions for RuO_2/CNT during oxygen evolution reaction (OER). We believe that this is due to the lower stability of a coating-like NaO_2 because of its noncrystalline nature and high electrode/electrolyte contact area. Although RuO_2/CNT catalyzes the decomposition of side products at a lower potential (3.66 V) compared to CNT (4.03 V), it cannot actively contribute to the main electrochemical reaction of the cell during OER ($\text{NaO}_2 \rightarrow \text{Na}^+ + \text{O}_2 + \text{e}^-$) because of the fast chemical degradation of the film NaO_2 to the side products. Therefore, tuning the morphology and crystallinity of NaO_2 by a catalyst is detrimental for the $\text{Na}-\text{O}_2$ cell performance and it should be taken into account for the future applications.



1. INTRODUCTION

Metal– O_2 batteries have attracted considerable attention as potential alternatives to the currently used Li-ion batteries for future electric vehicles because of their high theoretical energy density.^{1,2} Among all metal– O_2 batteries, Li– O_2 batteries are the most studied systems to date, in which Li_2O_2 reversibly forms as the main discharge (DC) product. However, the large overpotential of oxidation of the insulating Li_2O_2 (typically >1 V) compels low Coulombic efficiency and electrolyte decomposition to the cell, retarding their practical applications.^{2–4} For a few important merits, Li can be replaced by Na in metal– O_2 cells. Although $\text{Na}-\text{O}_2$ cells feature a lower theoretical energy density (1105 W h kg^{−1} based on NaO_2) than Li– O_2 cells (3500 W h kg^{−1} based on Li_2O_2), Na resources are much more abundant in nature and less expensive compared with Li, and the formation of NaO_2 as the main DC product results in a much lower charge overpotential (typically <0.2 V) because of faster oxygen

evolution reaction (OER) kinetics of the superoxide species.⁵ However, electrochemically formed NaO_2 is unstable in the cell environment and dissolves into Na^+ and highly active O_2^- , and the latter promotes time-dependent side products' formation by attacking the organic electrolyte and carbonaceous cathode.⁶ In this regard, a series of works investigated the effect of NaO_2 degradation on the cell electrochemistry. It was concluded that increasing the exposure time of NaO_2 to the electrolyte results in the elevated side products' (Na_2O_2 , $\text{Na}_2\text{O}_2 \cdot 2\text{H}_2\text{O}$, Na_2CO_3 , NaF, etc.) formation and consequently a precipitous increase in the charging overpotential.^{6,7}

A key question that remains unanswered is the effect of the catalyst on these complicated chemical/electrochemical reactions. Various catalysts including carbonaceous materi-

Received: June 24, 2018

Revised: July 30, 2018

Published: August 6, 2018

als,^{8,9} metals,^{10–12} and metal oxides^{13,14} have been developed in Na–O₂ batteries by different research groups. Recently, Sun et al. and Wu et al., respectively, showed the effect of Co₃O₄/carbon nanotube (CNT) and micrometer-sized RuO₂/boron-doped reduced graphene oxide (m-RuO₂/B-rGO) catalysts on the composition and morphology of the NaO_x (NaO₂/Na₂O₂) DC product in Na–O₂ batteries and their relatively improved performance compared to bare CNT and rGO.^{15,16} Also, Kang et al. reported the formation of deficient sodium peroxide (Na_{2–x}O₂) by using the Ru/CNT catalyst with a stable cycling performance for over 100 cycles.¹² On the other hand, in a series of publications, it is shown that the adsorption energy of catalysts toward the O₂[–] species is the key descriptor determining the catalytic activity and the cell overpotential in Na–O₂ batteries by both theoretical and experimental results.^{17,18} To date, NaO₂ is routinely observed as the primary DC product of Na–O₂ batteries. However, none of the aforementioned studies have considered NaO₂ degradation and its instability on the cell performance after using a catalyst. Therefore, mechanistic insights into the effect of a catalyst on NaO₂ characteristics and their interplay with NaO₂ stability and side products' formation are required.

In this paper, RuO₂ nanoparticles (NPs) have been used as the catalyst for Na–O₂ batteries in order to explore the effect of morphology and crystallinity of NaO₂ on its stability. We demonstrate: (i) the formation of a poorly crystalline NaO₂ film on RuO₂/CNT during oxygen reduction reaction (ORR), (ii) the low crystallinity and high electrolyte/electrode contact area of the deposited film reduces NaO₂ stability, (iii) and, consequently, accelerated side products' formation deleteriously increases charge potential. Our theoretical results support the weaker interaction between the NaO₂ component and graphitic carbon layer of the electrode in comparison to RuO₂ in the beginning of the ORR. According to our experimental results, tuning morphology and crystallinity of NaO₂ by using a catalyst has negative effects on the Na–O₂ battery behavior. Although the catalyst can decompose the side products at a lower charging potential compared to a catalyst-free cathode, it cannot reversibly catalyze the cell's main reaction during charge, and, therefore, the use of a catalyst is denied for superoxide-based Na–O₂ batteries.

2. EXPERIMENTAL SECTION

2.1. RuO₂/CNT and CNT Cathode Preparation. RuO₂/CNT composite was prepared through a facile microwave-assisted hydrothermal synthesis method. Pristine CNT (20 mg, >95% purity, diameter ≈ 20 nm, Sigma-Aldrich) was dispersed in 20 mL deionized (DI) water by using a 30 min bath sonication. Then, 40 mg of RuCl₃·xH₂O (99.9%, Alfa Aesar) was dissolved in the solution by vigorous stirring for another 30 min. The resulting mixture was transferred to a vessel, and microwave-assisted hydrothermal reaction was performed at 180 °C for 30 min in a microwave synthesis reactor (Anton Paar Monowave 300). After the reaction was performed, the resulting powder was washed and centrifuged with DI water and ethanol at least 5 times and dried in an oven at 60 °C overnight. Finally, the resulting RuO₂/CNT powder was annealed at 150 °C for 1 h in an ambient atmosphere. The amount of RuO₂ in the sample was ~31 wt %, obtained by thermal gravimetric analysis (result is not shown). For cathode preparation, RuO₂/CNT was ground with pristine CNT with the mass ratio of 6:4 and dispersed in isopropanol by 15 min tip sonication, and ~0.3 mg of the powder was deposited on

top of the pressed Ni-foam (~12 mm diameter) for battery measurements. The freestanding and binder-free film cathodes were prepared by vacuum filtration of the resulting slurries. After drying at 60 °C, the films were peeled off from the glassy fiber C (GF/C, Whatman) and dried under vacuum at 70 °C overnight prior to use. CNT cathodes and freestanding films were also prepared by the same procedures. The diameter and mass of the resulting films were 12 mm and ~3.6–3.8 mg, respectively. The weight of cathodes was measured using a microbalance with an accuracy of 0.01 mg. The freestanding and binder-free film cathodes were only used for X-ray diffraction (XRD) measurements, and for all of the other characterizations, the deposited Ni-foam cathodes were used with a cathode loading of ~0.3 mg.

2.2. Na–O₂ Cell Assembly and Cycling. All the procedures during cell assemblies were carried out in an Ar-filled glove box (O₂ level < 0.5 ppm, H₂O level < 0.5 ppm). The cathodes and Na–O₂ cell components were dried at 70 °C in a vacuum oven overnight before cell assemblies. The Na–O₂ cells were composed of a metallic Na-covered (ACS Reagent, Sigma-Aldrich) stainless-steel plate as the anode electrode, Celgard 2500 and GF/C (Whatman) as the separator, RuO₂/CNT or CNT as the cathode electrodes, and 280 μL of the electrolyte. The electrolyte was prepared with tetraethylene glycol dimethyl ether (>99%, Sigma-Aldrich), which contained 0.5 M NaCF₃SO₃ (NaOTf, 98%, Sigma-Aldrich). The salt was purified according to the procedure reported by McCloskey et al.,¹⁹ and the solvent was dried using 3 Å molecular sieves for over 7 days. The water amount of the final electrolyte was <10 ppm according to Karl Fischer titration.

Electrochemical examinations of the Na–O₂ cells were conducted using a battery cycler (Landt Instruments, CT2001A) after at least 8 h of relaxation under Ar atmosphere and 3 h of relaxation under a 1.5 atm of O₂ pressure (40 mL of volume capacity-integrated O₂ tank). The specific capacities and current densities were calculated according to the total mass of active materials (CNT and RuO₂/CNT) on the cathodes. For example, the absolute capacitance value for the experiments with a cutoff capacitance of 1000 mA h g^{–1} was 0.3 mA h. All of the reported plateau potentials are calculated by dividing the integral of the DC/recharge (RC) curves by their corresponding specific capacities. For cycling measurements, $E_{RC\ avg}$ values are also calculated by the same way for the whole RC window (1000 mA h g^{–1}) in each cycle.

2.3. Gas Consumption and Evolution Profile Measurement. To monitor the consumption of O₂ gas during DC and evolution of gaseous product during RC in the Na–O₂ cell operation, a custom-built on-line electrochemical mass spectrometry (OEMS) device was used. For the OEMS test, the cell was assembled in an Ar-filled glovebox. The cell was composed of a metallic Na-covered stainless-steel plate as the anode, GF/D and GF/C as separators, and RuO₂/CNT or CNT as the cathode. The electrolyte (300 μL) was used, composed of 0.5 M NaOTf containing tetraethylene glycol dimethyl ether. The cell components were stacked in the described order in a custom-made OEMS cell that has a small head part volume (~3.2 mL). The OEMS cell configuration (custom-designed with Tomcell, Japan) is similar to that of the standard Na–O₂ cell used for the general electrochemical testing, except for a considerably smaller headspace volume with inlet/outlet ports for gas. The cell headspace was calibrated through a volume calibration technique, where a

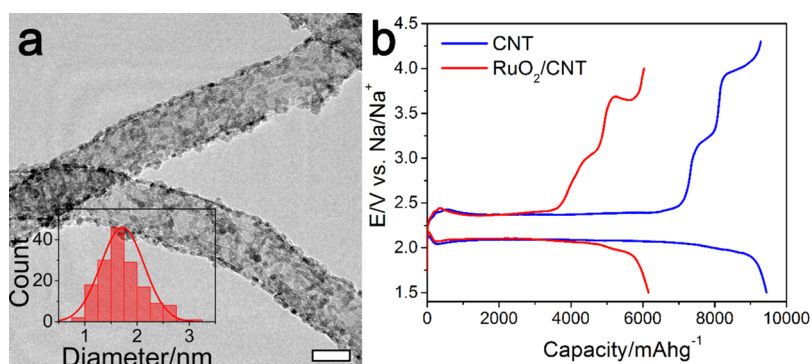


Figure 1. RuO₂/CNT electrode and Na–O₂ cell profile. (a) TEM image of RuO₂/CNT and RuO₂ particle size distribution over the CNTs (scale bar indicates 10 nm). (b) First DC/RC curves of the CNT (blue) and RuO₂/CNT (red) at a current density of 100 mA g^{−1} and DC cutoff potential of 1.5 V.

series of known volume loops were attached in place of the cell and pressurized to the same pressure. The details of volume calibration have been described in our previous reports.^{20,21} After assembly, the cell was placed in an incubator to maintain the temperature of the cell at 25 °C. Then, the cell was connected to the OEMS device, purged, and filled with high-purity O₂ gas (99.999%) and isolated from the gas supply line. The DC process was carried out in galvanostatic mode using a potentiostat (WPG100e, Wonatech) while monitoring the pressure change inside the cell using a high-precision pressure transducer (MMA030VSP3A6T3ASCE, Omega Engineering), which is connected to the cell. After DC, the cell was purged and refilled with Ar gas (99.999%). The recharging process was followed in galvanostatic mode, whereas the evolving gas was accumulated inside the isolated cell and sampled to a mass spectrometer (RGA200, Stanford Research Systems) every 30 min to analyze the composition of the accumulated gas. The pressure change during RC was also monitored with the pressure transducer connected to the cell. After the measurement, all the data were calculated for quantitative gas analysis.

2.4. Rotating Ring Disk Electrode Experiments. The rotating ring disk electrode (RRDE) has a glassy carbon disk electrode (GC, $d = 4$ mm) and surrounding gold ring electrode (Au, i.d. = 5 mm, o.d. = 7 mm). On the GC disk, either CNT or RuO₂/CNT was deposited by drop-casting their inks. The CNT and RuO₂/CNT inks were prepared by sonicating a 3 mL mixture of 8 mg of CNT or RuO₂/CNT, 40 μ L of Nafion (5 wt %, Ion Power, D520), and 2.96 mL of *N*-methyl-2-pyrrolidone (99%, Sigma-Aldrich) until obtaining a homogeneous dispersion. An aliquot of 4 μ L ink was dropped on the GC and dried at 60 °C under vacuum. Voltammetry for the Na–O₂ reaction was conducted in a bulk-electrolysis cell comprising the RRDE, Pt coil, and Pt wire as working, counter, and reference electrodes, respectively, dipped in an electrolyte of 0.5 M NaOTf dissolved in tetraglyme. The potential of the pseudo-reference electrode of the Pt wire was calibrated by measuring the voltage with respect to the Na metal affixed to the Ni wire in 0.5 M NaOTf/tetraglyme at open circuit, resulting in the potential of the Pt wire of 2.38 V with respect to the Na⁺/Na potential. Although the potential of the disk was swept in an initial cathodic direction at 2 mV/s in the potential range of −0.9 to 1.5 V (vs Pt, corresponding to 1.48–3.88 V vs Na⁺/Na), the constant potential of 0.6 V (vs Pt, corresponding to 2.98 V vs Na⁺/Na) was applied to the Au ring to detect the solvated O₂[−] and/or NaO₂. All the electrochemical tests were carried out in an Ar-filled glove box.

2.5. Further Characterization Methods. Discharged or charged cathodes were extracted from the disassembled Na–O₂ cells inside the Ar-filled glove box and washed with at least 3 mL of acetonitrile (anhydrous, >99.9%, Sigma-Aldrich) in order to remove the residual electrolyte and dried under vacuum without exposure to air. Morphological and structural characterizations were performed by scanning electron microscopy (SEM, FEI-Quanta 200 FEG) operating at 5 kV and transmission electron microscopy (TEM, FEI Tecnai G2 F30) operating at 100 kV. For the TEM sample preparation, fully discharged cathodes were scratched, and the resulting powders were applied on a lacy carbon-coated TEM copper grid. XRD patterns were collected using a PANalytical instrument (X'pert Pro MPD, Cu K α radiation, $\lambda = 1.5405$ Å). The XRD patterns were collected over the 2θ range of 30–50° using a Kapton tape for isolating the samples from air exposure, and the sample holder was spinning with the evolution time of 2 s during the measurements. High-resolution X-ray photoelectron spectroscopy (XPS, Thermo-scientific, K- α , Al K α radiation) was performed on pristine and cycled cathodes, and Raman spectra were collected on a confocal Raman instrument (WITec alpha300) by using an air tight sample holder. ¹H NMR spectroscopy was performed using a 400 MHz Bruker NMR system. The samples after DC or partial/complete charge were immersed in 0.6 mL of D₂O (Sigma-Aldrich) under Ar atmosphere, and the resulting solutions were collected for the measurements.

2.6. Theoretical Calculations. The numerical simulations of the graphene/NaO₂ and RuO₂/NaO₂ interfaces were conducted within the density functional theory (DFT) framework using the gradient-corrected approximation²² for the exchange–correlation functional and ultrasoft pseudopotentials²³ to model the interaction between the nuclei and electrons. The open-source code suite Quantum Espresso²⁴ was used to perform the calculations. A 40 Rydberg kinetic energy cutoff for the planewave expansion was used. The adhesion energy for the RuO₂/NaO₂ interface was calculated in a periodic, heterostructure geometry of alternating RuO₂ and NaO₂ layers of various thicknesses. All the calculations include spin polarization.

$$E_{\text{ad}} = [E_{\text{tot}} - nE_{\text{RuO}_2} - mE_{\text{NaO}_2}]/A \quad (1)$$

where E_{tot} is the total energy of the heterostructure and E_{RuO_2} and E_{NaO_2} are the energies of formula units' bulk RuO₂ and NaO₂, each consisting of three atoms, respectively. A is the

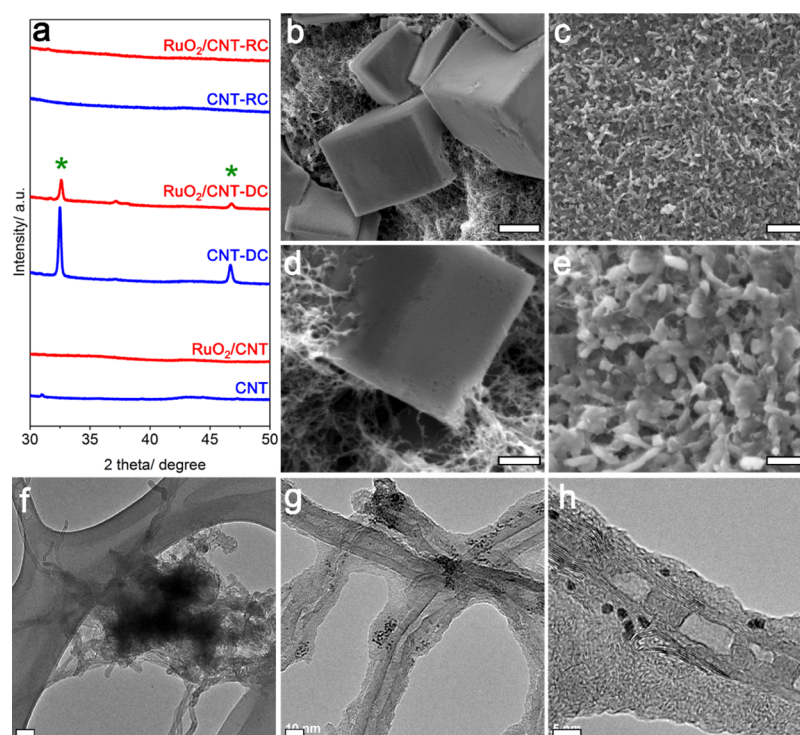


Figure 2. NaO₂ crystal and morphology characterization on the CNT and RuO₂/CNT. (a) XRD patterns of the CNT (blue) and RuO₂/CNT (red) at different states of: as-prepared (bottom), first-discharged (DC, middle), and first-recharged (RC, up), with a limited capacity of 1.5 mA h. The symbol * denotes NaO₂ reflections. (b–e) SEM images of the CNT-DC (b,d) and RuO₂/CNT-DC (c,e). Scale bars indicate (b,c) 2 μm and (d,e) 500 nm. (f–h) TEM images of DC (f) CNT and (g,h) RuO₂/CNT cathodes. Scale bars indicate (f) 50, (g) 10, and (h) 5 nm.

cross-sectional area of the interface. Finally, n and m are the numbers of formula units in the heterostructure model, constructed along the (001) direction of both the materials considered. Because of the lattice mismatch between the two crystals, an intermediate lattice constant of $a = 5.004$ Å was chosen. With this lattice constant, RuO₂ experiences a tensile strain of 12.08%, whereas NaO₂ is subjected to a compressive strain of 9.74%. The formula unit energies of the two bulk structures used in eq 1 were calculated under their respective strains.

The graphene/NaO₂ interface was constructed in a similar manner in a heterostructure geometry. A four-layer NaO₂ was followed by a single-layer graphene in an alternating arrangement along the direction of the normal to the interface. The interface energy in this case was calculated using

$$E_{\text{ad}} = [E_{\text{tot}} - nE_{\text{C}} - mE_{\text{NaO}_2}]/(2A) \quad (2)$$

where the definitions are similar to eq 1, with the exception of E_{C} , which is the energy of a single C atom in pristine graphene. The factor of two in the denominator is necessary to compensate for the double-sided interface. In this case, to mitigate the interfacial strain, we use a 40-atom rectangular graphene simulation cell and extend it by 3.45 and 11.99% along the two interface axes to match the calculated NaO₂ lattice constant of 5.54 Å.

3. RESULTS AND DISCUSSION

The RuO₂/CNT composite was synthesized through a one-pot microwave-assisted hydrothermal reaction. TEM images of the prepared composite show the uniform distribution of RuO₂ NPs with an average diameter of 1.72 nm on the CNT surface (Figures 1a and S1). The C 1s XPS spectrum of RuO₂/CNT

(Figure S2a,b) exhibited one pair of Ru 3d doublet for RuO₂, alongside C 1s peaks corresponding to CNT. The Raman spectrum of RuO₂/CNT consists of the well-known D-, G-, 2D-, and D + G-bands of CNT and two peaks at 520 and 631 cm⁻¹ relating to the first-order E_g and A_{1g} phonon bands of rutile RuO₂ (Figure S2c). Both CNT and RuO₂/CNT electrodes presented the same uniform pore size and distribution with entangled micron-sized CNTs (Figure S3).

Binder-free cathodes (CNT and RuO₂/CNT) drop-casted on Ni-foam were utilized in Na–O₂ cells with a 0.5 M sodium triflate (NaOTf)/tetraglyme electrolyte (<10 ppm of H₂O measured by Karl Fischer titration). A galvanostatic DC/RC measurement of the first cycles at 100 mA g⁻¹ current density in Figure 1b shows that RuO₂/CNT delivered a lower specific capacity (6157 mA h g⁻¹) compared to CNT (9444 mA h g⁻¹) at the end of DC with the cutoff potential of 1.5 V. The film NaO₂ growth on RuO₂/CNT during DC and blocking the active surface sites may be the reason for the lower capacity of RuO₂/CNT (will be discussed in Figure 2). During RC, three distinct regions were observed for both cathodes: (i) a plateau around 2.38 V, corresponding to NaO₂ decomposition,²⁵ (ii) a short slope between 3 and 3.3 V, and (iii) a plateau above 3.5 V, in which regions (ii) and (iii) are corresponding to the decomposition of side products, mainly Na₂O₂·2H₂O, NaOH, sodium carbonates, and sodium carboxylates.^{26,27} A detailed analysis of identifying the products responsible for each plateau is presented in the Supporting Information (Figures S4–S8). For regions (ii) and (iii), respectively, around 0.357 and 0.336 V charging potential reductions were found in the RC curve of RuO₂/CNT compared with CNT, implying that RuO₂ actively contributes to the decomposition of side products during OER. A more detailed analysis of the effect of RuO₂ on DC and RC

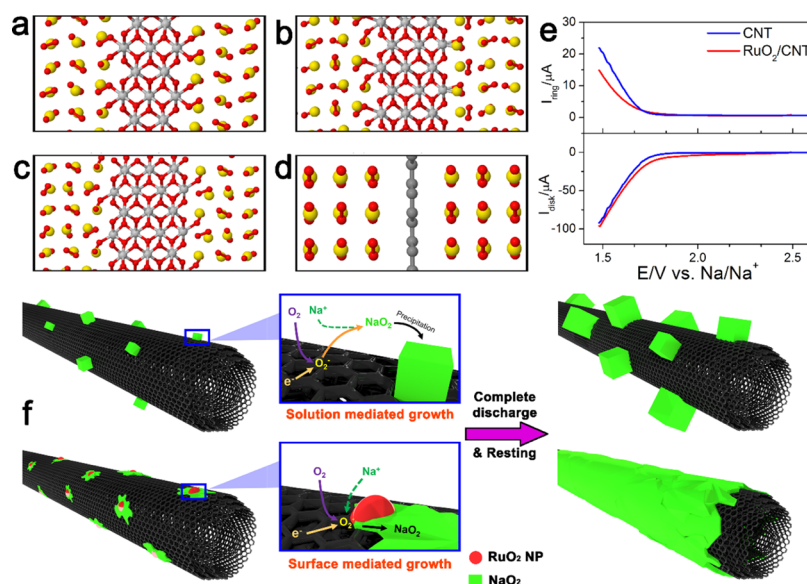


Figure 3. Mechanistic study for ORR. (a) Five-, (b) six- and (c) seven-layer RuO₂/NaO₂ interfaces along with the (d) single-layer graphene/four-layer NaO₂ interface. Yellow, red, gray, and black spheres indicate Na, O, Ru, and C atoms, respectively. (e) RRDE measurements with the cathodic voltammogram. Top and bottom panels display the Au ring current (i_{ring}) and disk electrode of RuO₂/CNT and CNT current (i_{disk}), respectively. RuO₂/CNT and the CNT loaded on the GC electrode were swept from 2.5 to 1.5 V with a scan rate of 2 mV s⁻¹ and a rotation rate of 900 rpm, whereas the Au ring electrode was held at a constant potential of 2.98 V vs Na/Na⁺ (0.6 V vs Pt RE) to detect O₂⁻. (f) Schematic illustration of NaO₂ nucleation and growth on the CNT and RuO₂/CNT cathodes.

behavior of the Na–O₂ cell will be presented in the subsequent parts of this work. It is noteworthy that region (iii) does not stand for electrolyte decomposition, as no plateau was observed during RC of fresh cells (Figure S9) in which the extracted currents are believed to be due to the electrolyte decomposition.

In the next step, we analyzed the identity, crystallinity, and morphology of the DC product in CNT and RuO₂/CNT cathodes. The appearance of an intense Raman band at 1156 cm⁻¹ in the Raman spectra of the DC samples indicates the deposition of NaO₂ as the main product during ORR, which disappears in the subsequent RC cathodes by decomposition during OER (Figure S10). The effect of the RuO₂ catalyst on the crystallinity of the NaO₂ DC product was explored by XRD on pristine, DC, and RC cathodes (Figure 2a). The patterns of DC cathodes consist of mainly two peaks at $2\theta = 32.5^\circ$ and 46.6° relating to the (200) and (220) reflections of NaO₂ (ICSD 98-008-7177), respectively, which vanish in the RC cathodes. However, the crystallinity of NaO₂ considerably differed in the DC CNT and DC RuO₂/CNT. According to the (200) reflection peak of NaO₂, the area under the peak in the DC RuO₂/CNT cathode was ~31% of that in the DC CNT cathode. Assuming the deposition of the same amount of NaO₂ in both DC cathodes at a fixed capacity of 1.5 mA h, ~69% reduction of the peak area suggests less crystalline NaO₂ in the presence of RuO₂ NPs.

In order to further probe the NaO₂ morphology change triggered by the RuO₂ catalyst, DC cathodes were explored by SEM and TEM. The DC CNT cathode contained well-defined micron-sized cubic NaO₂ (Figure 2b,d), compatible with the observation of Hartmann et al.²⁵ Instead, drastic morphological changes were observed in the DC RuO₂/CNT with the formation of film-like NaO₂ without any cubic particles (Figure 2c,e). TEM images of the DC CNT cathode clearly show bulk NaO₂ particle anchoring on CNTs with clean side walls (Figures 2f and S11). The crystalline nature of these particles

was further approved by the selected area electron diffraction (SAED) pattern (Figure S11b), in which all the diffraction d -spacing values can be assigned to NaO₂ (ICSD 98-008-7177). This feature was distinguished from NaO₂ observed in the DC RuO₂/CNT, in which a conformal NaO₂ film was observed on the cathode without any exposed bare electrode surface left (Figures 2g and S11). The high-resolution TEM image (Figure 2h) clearly indicates the amorphous nature of the deposited NaO₂ film, which was also confirmed by observing no diffraction from NaO₂ in the SAED pattern of the DC RuO₂/CNT (Figure S11d). NaO₂ was completely decomposed after RC, and the cathodes preserved their original morphology after the first DC and RC (Figure S7c,f).

To provide an atomistic scale understanding of the differences in the interaction of the NaO₂ component with the CNT and RuO₂, we conduct DFT calculations. We model the CNT surface using a graphene layer, as the CNT radii are large enough to ignore the curvature effects. The geometry-optimized RuO₂/NaO₂ and the graphitic layer of the carbon electrode, that is, graphene/NaO₂ interfaces are depicted in Figure 3a–d. During optimization, the NaO₂ component undergoes extensive structural distortions in both the RuO₂/NaO₂ and graphene/NaO₂ interfaces. In particular, the bonded oxygen pairs execute free rotations. These structural distortions, initiated at the interface, propagate with facility deep into the NaO₂ bulk regions. The oxygen atoms at the NaO₂ side of the interface form strong covalent bonds with the Ru atoms with Ru–O bond distances of approximately 2.3 Å, only slightly larger than the Ru–O lengths in bulk RuO₂. The RuO₂ component, on the other hand, mostly maintains its bulk structure. To check the convergence of the adhesion energies with respect to the NaO₂ and RuO₂ thicknesses, calculations were conducted on three different interface geometries, namely, with five, six, and seven layers of NaO₂ and RuO₂ (Figure 3a–c). In the case of the graphene/NaO₂ interface (Figure 3d), the interfacial interaction was found to be of a

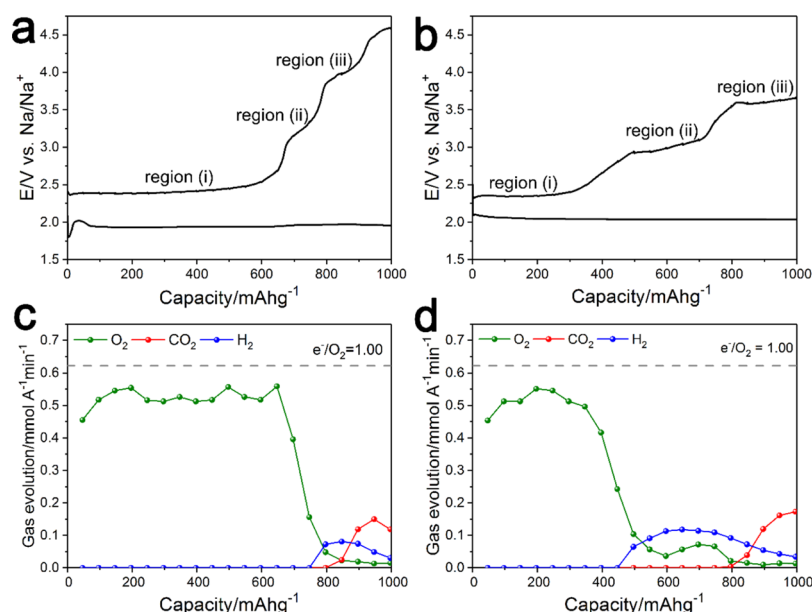


Figure 4. Galvanostatic DC/RC curves and the corresponding OEMS profiles during RC of (a,c) the CNT and (b,d) RuO₂/CNT. Three different plateaus of decomposition of NaO₂ [region (i)] and the side products [regions (ii) and (iii)] are identified on the RC curves. The quantitative gas analysis profiles show O₂, CO₂, and H₂ evolution at 100 mA g⁻¹ current density with a limited capacity of 1000 mA h g⁻¹. The horizontal dashed lines indicate the ideal 1 e⁻/O₂.

weaker nature. No chemical bonds were formed across the interface and as a result, the interface-initiated distortions in the NaO₂ component were observed to be significantly smaller. Because of this weak interlayer interaction, the behavior of this interface is expected to resemble the actual multilayer graphene/NaO₂ interface in our experiments. The calculated adhesion energies are collected in Table S1. According to our theoretical calculations, the ranges of interaction energies relevant to the two types of interfaces at hand are widely different. Whereas NaO₂/RuO₂ reflects a strong chemical bond formation with its adhesion energy in excess of -7 J/m², the adhesion energy characterizing the graphene/NaO₂ interface is an order of magnitude smaller, consistent with a weak interaction. Our results also reflect a satisfactory convergence for the NaO₂/RuO₂ adhesion energies at the seven-layer level.

This computational envision is also supported by RRDE measurements for ORR (Figure S12). Figure 3e shows the disk-electrode current (i_{disk}) of the CNT (blue) and RuO₂/CNT (red), and the corresponding Au ring current (i_{ring}) in the bottom and top panels, respectively, when a cathodic linear sweep voltammogram was performed. The RuO₂/CNT disk electrode exhibits an onset potential that is ~ 50 mV more positive than CNT. This result indicates the catalytic effect of the RuO₂ NP for ORR ($\text{O}_2 + \text{e}^- \rightarrow \text{O}_2^-$). With a forward cathodic potential sweep, the increasing i_{disk} has an influence on the i_{ring} , which is responsible for the solvation of superoxide species ($\text{O}_2^-(\text{sol}) \rightarrow \text{O}_2 + \text{e}^-$). It indicates the decreased portion of NaO₂ deposition on the disk electrode with increasing cathodic potential. Notably, the i_{ring} appearing for RuO₂/CNT is lower than that for the CNT, despite the relatively higher i_{disk} , which demonstrates a stronger adsorption affinity of superoxide species to the RuO₂ NP than the CNT, leading to prompt passivation of the RuO₂ surface by NaO₂.

Taken together, the effect of the RuO₂ catalyst during ORR can be accounted for using the following ORR process



where the asterisk symbol (*) demonstrates the surface adsorption. Because of the high adsorption affinity of O₂^{*} toward RuO₂ NPs, steps 3–5 and the following lateral growth of NaO₂ occur in the proximity of RuO₂ in the beginning of DC. According to our results, there is a relatively strong binding of O₂^{*} to the RuO₂ NP ($\text{RuO}_2 \cdots \text{O}_2^*$), which suppresses a decent Na–O₂^{*} binding; therefore, structural defects (like Na vacancies) in the final NaO₂ can be expected, resulting in a poorly crystalline product. As a result, the deposition of NaO₂ is carried out on the RuO₂ NP surface in the following DC process (Figure 3f), and the DC overpotential increases as the lateral growth continues on the bare CNT. It is noteworthy that in the absence of RuO₂ NP, steps 3 and 4 take place apart from step 5, linked by O₂⁻ dissolution through the electrolyte to the already precipitated NaO₂ (Figure 3f), which is known as the solution-mediated route and is responsible for the formation of micron-sized insulating NaO₂ cubes.²⁸ It is distinct from the surface-mediated route happening on the topmost surface of RuO₂, in which the fraction of dissolved species in the electrolyte is relatively lower and the film-like morphology is observed, as demonstrated by RRDE (Figure 3e) and microscopy images (Figure 2b–h), respectively.

The subsequent RC process with different shapes and structures of NaO₂ was investigated by gas analysis. Both the CNT and RuO₂/CNT cells were assessed using OEMS after the examination with a fixed DC capacity (1000 mA h g⁻¹). Figure 4 shows the first DC and RC profiles linked with OEMS results at a constant capacity of 1000 mA h g⁻¹. The DC potential (1.95 V) of the CNT (Figure 4a) in the OEMS cells is slightly lower than the one with full capacity measurement (~ 2.05 V, Figure 1b), which, however, insignificantly affects the following RC process. In region (i), the sole gaseous product of O₂ evolves (Figure 4c,d), which accounts for the

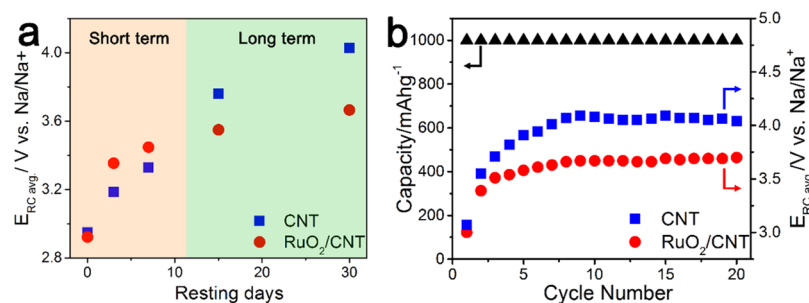


Figure 5. Na–O₂ cell stability measurements. (a) Results of charging potentials vs resting spans for the samples rested for 0–30 days between DC and RC, extracted from Figure S12. The time domain is divided into short and long terms, in which the RuO₂/CNT cathode exhibits higher and lower RC average potentials than the CNT, respectively. (b) Cycling performance of the CNT and RuO₂/CNT with a current density of 100 mA g⁻¹ and a limited capacity of 1000 mA h g⁻¹. The black triangles (linked to the left y-axis) show the capacity of both the cathodes during cycling and the blue squares and red circles (linked to the right y-axis) indicate the average RC potential during cycling for the CNT and RuO₂/CNT, respectively.

predominant NaO₂ decomposition at this region. However, the capacity retention for region (i) is markedly lower for the RuO₂/CNT electrode (~ 400 mA h g⁻¹) than the CNT (~ 700 mA h g⁻¹), which corresponds to the smaller quantity of O₂ evolution (Figure S13). Instead, RuO₂/CNT shows the elongated second and third potential plateaus at regions (ii) and (iii), when H₂ and CO₂ gases evolve, respectively, and the O₂ gas amount is pronouncedly decreased. The result of gas analysis indicates the termination of NaO₂ decomposition, followed by the stepwise decomposition of the side products. Pinedo et al. suggested the origin of H₂ evolution from the decomposition of Na₂O₂·2H₂O and NaOH.²⁹ The evolution of CO₂ gas at the end of RC stems from the oxidation of sodium carbonates, which may arise from degradation of the electrolyte solution and CNT electrode by the solvated O₂⁻.^{6,7} Therefore, larger amounts of H₂ and CO₂ gas evolution than CNT indicate the formation of a larger quantity of these side products, which is the drawback of film-shaped and noncrystalline NaO₂ formed in RuO₂/CNT. The high surface area of the NaO₂ film facing the electrolyte solution and the CNT electrode is facily involved in the side reactions. In addition, because of the weak interaction of NaO₂, the superoxide species can facily dissolve from the bulk film of noncrystalline NaO₂, which promotes degradation and side reactions. This behavior is distinguished from the initial deposition of NaO₂ to RuO₂ NP with the high adsorption affinity. The other remarkable feature is the lower potential of region (iii) than the one for CNT, implicating the fast decomposition of sodium carbonates by RuO₂ NPs.

To demonstrate such a catalytic effect of RuO₂ NPs for the decomposition of sodium carbonates, we elongated the resting time after DC. The superoxide species dissolved from NaO₂ leads to unintended chemical reactions, which are dependent on the resting time before starting RC. As shown in Figure S14, resting up to 30 days led to a decrease of the RC capacity for region (i). After 3 days of resting, the potential of region (i) rises to 2.75 V for RuO₂/CNT and the capacity pronouncedly shortens to <50 mA h g⁻¹, which implies almost complete transformation of NaO₂ to side products. The capacity retention for region (i) sustains more for the CNT electrode, whereas this plateau eventually disappears after 30 days. Similarly, we also found shrinkage of the region (i) period when the current rate was lower (Figure S15). All these results corroborate serious chemical side reactions when NaO₂ products are sitting on the electrode, and the correlation of

average RC potentials with resting spans is summarized in Figure 5a. By around 10 days of resting as indicated by a short term, a greater increment of RC potential was observed for RuO₂/CNT (0.53 V) compared to the CNT (0.38 V). Over 10 days, the average RC potential for RuO₂/CNT is moderately increased and lower than that for the CNT. During this long-term resting, region (iii) is prominent possibly due to the most existence of sodium carbonates. The low potential of region (iii) at ~ 3.75 V is attributed to the catalytic effect of RuO₂ NPs for decomposition of sodium carbonates. In contrast, the CNT electrode shows the shrinking of region (i) and no catalytic effect in region (iii) (~ 4 V), which overall raises the average RC potential. Sun et al. and Wu et al. reported tuning the properties (morphology, composition, structure) of the NaO_x (NaO₂/Na₂O₂) DC product in Na–O₂ batteries by Co₃O₄/CNT and m-RuO₂/B-rGO catalysts, respectively.^{15,16} The improved cells' performance was attributed to the catalytic activity toward the electrochemical decomposition of NaO_x and Na₂CO₃. In comparison, we demonstrate the effect of RuO₂ NPs that contribute to the formation of film-shaped and noncrystalline NaO₂ and fast decomposition of sodium carbonates. However, the catalytic effect of RuO₂ NP in Li–O₂ batteries is distinguished in the role of catalyst on decomposition of products during OER. Although in both battery systems, the catalyst actively contributes to the decomposition of carbonate species, the poorly crystalline Li₂O₂ film deposited by using RuO₂ NPs can be decomposed at lower potentials than the typical Li₂O₂ toroidal particles.^{30,31}

Last, the cycling performance of the RuO₂/CNT and CNT cathodes was examined using a cut-off capacity of 1000 mA h g⁻¹ at a 100 mA g⁻¹ current density (Figures 5b and S17). In the beginning five cycles, the average RC potentials were increased for both cathodes caused by accumulation of side products as reported by Black et al.³² However, RuO₂/CNT showed a stable RC potential at ~ 3.7 V for the subsequent cycles in contrast to the CNT at ~ 4.05 V. By investigating the 20-times-cycled cathodes with SEM, it can be seen that the accumulation of side products in the CNT cathode is more pronounced than in RuO₂/CNT, which is further confirmed by XPS C 1s spectra of the cycled cathodes. In the XPS spectrum, the CNT shows a higher ratio of functional decomposition groups: C–C compared with RuO₂/CNT (Figure S18). This result reveals that Na–O₂ batteries urge inevitable side reactions by superoxide species during cycling,

whereas the catalyst that rapidly oxidizes these sodium carbonates can lower the total RC potential.

4. CONCLUSIONS

In summary, the effect of the RuO₂/CNT catalyst on the Na–O₂ battery electrochemistry/chemistry was studied. RuO₂/CNT actively contributed to the formation of a film-like NaO₂, which is less crystalline than the cubic NaO₂ particles deposited on the CNT. The surface-mediated growth mechanism has been identified for depositing the coating-like NaO₂ in RuO₂/CNT by RRDE measurements. In contrast, the solution-mediated growth mechanism has been assigned for the formation of micron-sized NaO₂ cubes in the CNT, which is compatible with the literature. It turned out that the physical distinctions among film and cubic particle NaO₂ severely influence their stability during resting spans between DC and RC. The high electrode/electrolyte contact area of the film NaO₂ and its lower crystallinity favor more decomposition, elevated side products' formation, and RC overpotential increment for RuO₂/CNT during short resting spans. On the other hand, RuO₂ catalyzes side products' decomposition during OER, which exerts 0.37 V lower RC overpotential for side products' decomposition region compared to bare CNT and makes it a quite suitable catalyst for long resting times. However, the catalyst could not actively catalyze the main cell reaction during charge (NaO₂ → Na⁺ + O₂ + e[−]) because of the accelerated side products' formation from the coating-like NaO₂ chemical degradation. Therefore, the use of a catalyst for tuning superoxide morphology and crystallinity may not guide a proper strategy to improve an Na–O₂ battery performance. Nevertheless, the usage of a catalyst to prompt the decomposition of the side products may be necessary if unintended side reactions from superoxide species cannot be avoided.

■ ASSOCIATED CONTENT

Supporting Information

The Supporting Information is available free of charge on the ACS Publications website at DOI: 10.1021/acs.jpcc.8b06024.

Further SEM and TEM images of the as-prepared and discharged cathodes, electrochemical examinations, Raman, XPS, and NMR characterizations (PDF)

■ AUTHOR INFORMATION

Corresponding Author

*E-mail: yilmaz@unam.bilkent.edu.tr.

ORCID

Mohammad Fathi Tovini: 0000-0003-4334-4471

Daniele Toffoli: 0000-0002-8225-6119

Hande Ustunel: 0000-0003-0307-9036

Hye Ryung Byon: 0000-0003-3692-6713

Eda Yilmaz: 0000-0002-8365-838X

Author Contributions

E.Y. and M.F.T. designed the experiments. The battery measurements and material characterizations were performed by M.F.T. The RRDE and OEMS measurements were designed and performed by M.H., J.P., and H.R.B. Theoretical calculations were performed by M.D., D.T., and H.U. The article was written through contributions of all the authors. All the authors have given approval to the final version of the article.

Notes

The authors declare no competing financial interest.

■ ACKNOWLEDGMENTS

This study is financially supported by The Scientific and Technological Research Council of Turkey (TUBITAK) with the project number 115M375 and the National Research Foundation (NRF) of Korea (grant NRF-2016R1C1B2008690).

■ REFERENCES

- (1) Dunn, B.; Kamath, H.; Tarascon, J.-M. Electrical Energy Storage for the Grid: A Battery of Choices. *Science* **2011**, *334*, 928–935.
- (2) Bruce, P. G.; Freunberger, S. A.; Hardwick, L. J.; Tarascon, J.-M. Li-O₂ and Li-S Batteries with High Energy Storage. *Nat. Mater.* **2012**, *11*, 19–29.
- (3) Zhao, N.; Guo, X. Cell Chemistry of Sodium-Oxygen Batteries with Various Nonaqueous Electrolytes. *J. Phys. Chem. C* **2015**, *119*, 25319–25326.
- (4) Jiang, H. R.; Wu, M. C.; Zhou, X. L.; Yan, X. H.; Zhao, T. S. Computational Insights into the Effect of Carbon Structures at the Atomic Level for Non-Aqueous Sodium-Oxygen Batteries. *J. Power Sources* **2016**, *325*, 91–97.
- (5) Xia, C.; Fernandes, R.; Cho, F. H.; Sudhakar, N.; Buonacorsi, B.; Walker, S.; Xu, M.; Baugh, J.; Nazar, L. F. Direct Evidence of Solution-Mediated Superoxide Transport and Organic Radical Formation in Sodium-Oxygen Batteries. *J. Am. Chem. Soc.* **2016**, *138*, 11219–11226.
- (6) Kim, J.; Park, H.; Lee, B.; Seong, W. M.; Lim, H.-D.; Bae, Y.; Kim, H.; Kim, W. K.; Ryu, K. H.; Kang, K. Dissolution and ionization of sodium superoxide in sodium-oxygen batteries. *Nat. Commun.* **2016**, *7*, 10670.
- (7) Landa-Medrano, I.; Pinedo, R.; Bi, X.; de Larramendi, I. R.; Lezama, L.; Janek, J.; Amine, K.; Lu, J.; Rojo, T. New Insights into the Instability of Discharge Products in Na-O₂ Batteries. *ACS Appl. Mater. Interfaces* **2016**, *8*, 20120–20127.
- (8) Ma, J.-L.; Zhang, X.-b. Optimized Nitrogen-Doped Carbon with a Hierarchically Porous Structure as a Highly Efficient Cathode for Na-O₂ Batteries. *J. Mater. Chem. A* **2016**, *4*, 10008–10013.
- (9) Zhang, S.; Wen, Z.; Jin, J.; Zhang, T.; Yang, J.; Chen, C. Controlling Uniform Deposition of Discharge Products at the Nanoscale for Rechargeable Na-O₂ Batteries. *J. Mater. Chem. A* **2016**, *4*, 7238–7244.
- (10) Zhang, S.; Wen, Z.; Rui, K.; Shen, C.; Lu, Y.; Yang, J. Graphene Nanosheets Loaded with Pt Nanoparticles with Enhanced Electrochemical Performance for Sodium-Oxygen Batteries. *J. Mater. Chem. A* **2015**, *3*, 2568–2571.
- (11) Kumar, S.; Kishore, B.; Munichandraiah, N. Electrochemical Studies of Non-Aqueous Na-O₂ Cells Employing Ag-Rgo as the Bifunctional Catalyst. *RSC Adv.* **2016**, *6*, 63477–63479.
- (12) Kang, J.-H.; Kwak, W.-J.; Aurbach, D.; Sun, Y.-K. Sodium Oxygen Batteries: One Step Further with Catalysis by Ruthenium Nanoparticles. *J. Mater. Chem. A* **2017**, *5*, 20678–20686.
- (13) Rosenberg, S.; Hintennach, A. In situ formation of α-MnO₂ nanowires as catalyst for sodium-air batteries. *J. Power Sources* **2015**, *274*, 1043–1048.
- (14) Yin, W.-W.; Fu, Z.-W. A Highly Efficient Bifunctional Heterogeneous Catalyst for Morphological Control of Discharged Products in Na-Air Batteries. *Chem. Commun.* **2017**, *53*, 1522–1525.
- (15) Sun, Q.; Liu, J.; Li, X.; Wang, B.; Yadegari, H.; Lushington, A.; Banis, M. N.; Zhao, Y.; Xiao, W.; Chen, N.; et al. Atomic Layer Deposited Non-Noble Metal Oxide Catalyst for Sodium-Air Batteries: Tuning the Morphologies and Compositions of Discharge Product. *Adv. Funct. Mater.* **2017**, *27*, 1606662.
- (16) Wu, F.; Xing, Y.; Lai, J.; Zhang, X.; Ye, Y.; Qian, J.; Li, L.; Chen, R. Micrometer-Sized RuO₂ Catalysts Contributing to Formation of Amorphous Na-Deficient Sodium Peroxide in Na-O₂ Batteries. *Adv. Funct. Mater.* **2017**, *27*, 1700632.

- (17) Krishnamurthy, D.; Hansen, H. A.; Viswanathan, V. Universality in Nonaqueous Alkali Oxygen Reduction on Metal Surfaces: Implications for Li-O₂ and Na-O₂ Batteries. *ACS Energy Lett.* **2016**, *1*, 162–168.
- (18) Yadegari, H.; Banis, M. N.; Lushington, A.; Sun, Q.; Li, R.; Sham, T.-K.; Sun, X. A Bifunctional Solid State Catalyst with Enhanced Cycling Stability for Na and Li-O₂ Cells: Revealing the Role of Solid State Catalysts. *Energy Environ. Sci.* **2017**, *10*, 286–295.
- (19) McCloskey, B. D.; Garcia, J. M.; Luntz, A. C. Chemical and Electrochemical Differences in Nonaqueous Li-O₂ and Na-O₂ Batteries. *J. Phys. Chem. Lett.* **2014**, *5*, 1230–1235.
- (20) Wong, R. A.; Yang, C.; Dutta, A.; O, M.; Hong, M.; Thomas, M. L.; Yamanaka, K.; Ohta, T.; Waki, K.; Byon, H. R. Critically Examining the Role of Nanocatalysts in Li-O₂ Batteries: Viability toward Suppression of Recharge Overpotential, Rechargeability, and Cyclability. *ACS Energy Lett.* **2018**, *3*, 592–597.
- (21) Wong, R. A.; Dutta, A.; Yang, C.; Yamanaka, K.; Ohta, T.; Nakao, A.; Waki, K.; Byon, H. R. Structurally Tuning Li₂O₂ by Controlling the Surface Properties of Carbon Electrodes: Implications for Li-O₂ Batteries. *Chem. Mater.* **2016**, *28*, 8006–8015.
- (22) Perdew, J. P.; Burke, K.; Ernzerhof, M. Generalized Gradient Approximation Made Simple. *Phys. Rev. Lett.* **1996**, *77*, 3865–3868.
- (23) Giannozzi, P.; Baroni, S.; Bonini, N.; Calandra, M.; Car, R.; Cavazzoni, C.; Ceresoli, D.; Chiarotti, G. L.; Cococcioni, M.; Dabo, I.; et al. Quantum Espresso: A Modular and Open-Source Software Project for Quantum Simulations of Materials. *J. Phys.: Condens. Matter* **2009**, *21*, 395502.
- (24) Vanderbilt, D. Soft Self-Consistent Pseudopotentials in a Generalized Eigenvalue Formalism. *Phys. Rev. B: Condens. Matter Phys.* **1990**, *41*, 7892–7895.
- (25) Hartmann, P.; Bender, C. L.; Vračar, M.; Dürr, A. K.; Garsuch, A.; Janek, J.; Adelhelm, P. A Rechargeable Room-Temperature Sodium Superoxide (NaO₂) Battery. *Nat. Mater.* **2013**, *12*, 228–232.
- (26) Zhao, N.; Li, C.; Guo, X. Long-Life Na-O₂ Batteries with High Energy Efficiency Enabled by Electrochemically Splitting NaO₂ at a Low Overpotential. *Phys. Chem. Chem. Phys.* **2014**, *16*, 15646–15652.
- (27) Kwak, W.-J.; Chen, Z.; Yoon, C. S.; Lee, J.-K.; Amine, K.; Sun, Y.-K. Nanoconfinement of low-conductivity products in rechargeable sodium-air batteries. *Nano Energy* **2015**, *12*, 123–130.
- (28) Hartmann, P.; Heinemann, M.; Bender, C. L.; Graf, K.; Baumann, R.-P.; Adelhelm, P.; Heiliger, C.; Janek, J. Discharge and Charge Reaction Paths in Sodium-Oxygen Batteries: Does NaO₂ Form by Direct Electrochemical Growth or by Precipitation from Solution? *J. Phys. Chem. C* **2015**, *119*, 22778–22786.
- (29) Pinedo, R.; Weber, D. A.; Bergner, B.; Schröder, D.; Adelhelm, P.; Janek, J. Insights into the Chemical Nature and Formation Mechanisms of Discharge Products in Na-O₂ Batteries by Means of Operando X-ray Diffraction. *J. Phys. Chem. C* **2016**, *120*, 8472–8481.
- (30) Yoon, K. R.; Lee, G. Y.; Jung, J.-W.; Kim, N.-H.; Kim, S. O.; Kim, I.-D. One-Dimensional RuO₂/Mn₂O₃ Hollow Architectures as Efficient Bifunctional Catalysts for Lithium-Oxygen Batteries. *Nano Lett.* **2016**, *16*, 2076–2083.
- (31) Yilmaz, E.; Yogi, C.; Yamanaka, K.; Ohta, T.; Byon, H. R. Promoting Formation of Noncrystalline Li₂O₂ in the Li-O₂ Battery with RuO₂ Nanoparticles. *Nano Lett.* **2013**, *13*, 4679–4684.
- (32) Black, R.; Shyamsunder, A.; Adeli, P.; Kundu, D.; Murphy, G. K.; Nazar, L. F. The Nature and Impact of Side Reactions in Glyme-based Sodium-Oxygen Batteries. *ChemSusChem* **2016**, *9*, 1795–1803.